

## RESOLVING THE KINEMATIC DISTANCE AMBIGUITY TOWARD GALACTIC H II REGIONS

MICHAL A. KOLPAK, JAMES M. JACKSON, T. M. BANIA, AND D. P. CLEMENS  
Institute for Astrophysical Research, 725 Commonwealth Avenue, Boston University, Boston, MA 02215

AND

JOHN M. DICKEY  
Astronomy Department, 116 Church Street SE, University of Minnesota, Minneapolis, MN 55455

Received 2002 August 26; accepted 2002 September 17

### ABSTRACT

Kinematic distance determinations in the inner Galaxy are hampered by the near-far kinematic distance ambiguity. Here we resolve the ambiguity for 49 H II region complexes with known recombination-line velocities in the first Galactic quadrant. We measured the 21 cm H I absorption spectrum toward each source with the Very Large Array in the C array. The maximum velocity of H I absorption was used to discriminate between the near and far kinematic distances. The number ratio of far to near sources,  $\sim 3$ , can be entirely explained as a geometrical effect. The kinematic distances that we derive are compared with previous determinations for the same sources. Although our distance determinations are largely in agreement with previous measurements, there are 22 discrepancies that we discuss. Using our distance determinations, we create a face-on Galactic map of the H II region complexes and compare it with a kinematically derived profile of the distribution of CO-traced molecular hydrogen. The H II region complexes delineate the large-scale features seen in the molecular gas. The 5 kpc molecular ring and the Sagittarius spiral arm are clearly evident, and a few H II region complexes lie in the Perseus arm.

*Subject headings:* Galaxy: general — Galaxy: structure — H II regions — ISM: atoms —  
radio lines: ISM — techniques: spectroscopic

*On-line material:* additional figures

## 1. INTRODUCTION

### 1.1. Background

Distance measurements are fundamentally important to studies of the Galaxy. Distances are needed to establish the luminosity, size, and mass of Galactic sources and also to determine the face-on structure of the Galaxy. A method to determine distances on a Galactic scale accurately and unambiguously would be extremely valuable.

Distance determination for Galactic sources, however, is difficult. The most accurate parallax measurements to date were made using data from the *Hipparcos* mission and have standard errors of 1–2 mas (Perryman et al. 1995). This technique is therefore currently limited to distances of a few hundred parsecs. Water maser proper motion measurements have yielded very accurate distances to a few sources (e.g., W49, W51, and Sgr B2), but these studies require several years of observations and are limited to only a handful of sources. Determinations of kinematic distance, on the other hand, only require the measurement of the radial velocity of a source and the application of a Galactic circular rotation curve (e.g., Clemens 1985, hereafter C85). Although kinematic distance determinations are less direct than other methods, they can provide a distance estimate for any source of spectral-line radiation in the Galaxy.

Although determination of kinematic distances is straightforward in the outer Galaxy, it is problematic in the inner Galaxy because of the so-called kinematic distance ambiguity (KDA). In the inner Galaxy, along a given line of sight, each radial velocity value corresponds to two distances equally spaced on either side of the tangent point. Only sources at the tangent point have unambiguous distances.

This is a problem for all axisymmetric rotation curves and has been a significant obstacle to the determination of reliable kinematic distances (e.g., Clemens, Sanders, & Scoville 1988, hereafter CSS88).

Fortunately, this long-standing problem can be solved for many Galactic H II regions through measurement of their absorption spectra. If there is an interstellar cloud between an H II region and the observer, the thermal bremsstrahlung radio continuum emission from the background H II region is absorbed at frequencies corresponding to atomic and molecular transitions of the various gas species in the cloud. These absorption lines are Doppler shifted to the radial velocity of the absorbing cloud. If an H II region is located at its far kinematic distance, there can be absorption from clouds that have radial velocities up to and including the tangent-point velocity. If an H II region is located at its near kinematic distance, however, there can only be absorption from clouds that have radial velocities less than the radial velocity of the background H II region. Therefore, a measurement of the maximum velocity of absorption can be used to discriminate between near and far sources, provided that the velocity of the H II region is known and there are several absorbing clouds along the line of sight.

Figure 1 illustrates this KDA resolution technique with a schematic example. In Figures 1a and 1c, we show face-on schematic diagrams of the Galaxy, drawn from the perspective of the north Galactic pole (the Galaxy rotates clockwise). The concentric, shaded annuli represent example concentrations of cold, clumpy H I, the circled asterisks represent H II region complexes, and the long, diagonal lines indicate the lines of sight. The places where the sight lines intersect H I clouds are numbered in the face-on diagrams.

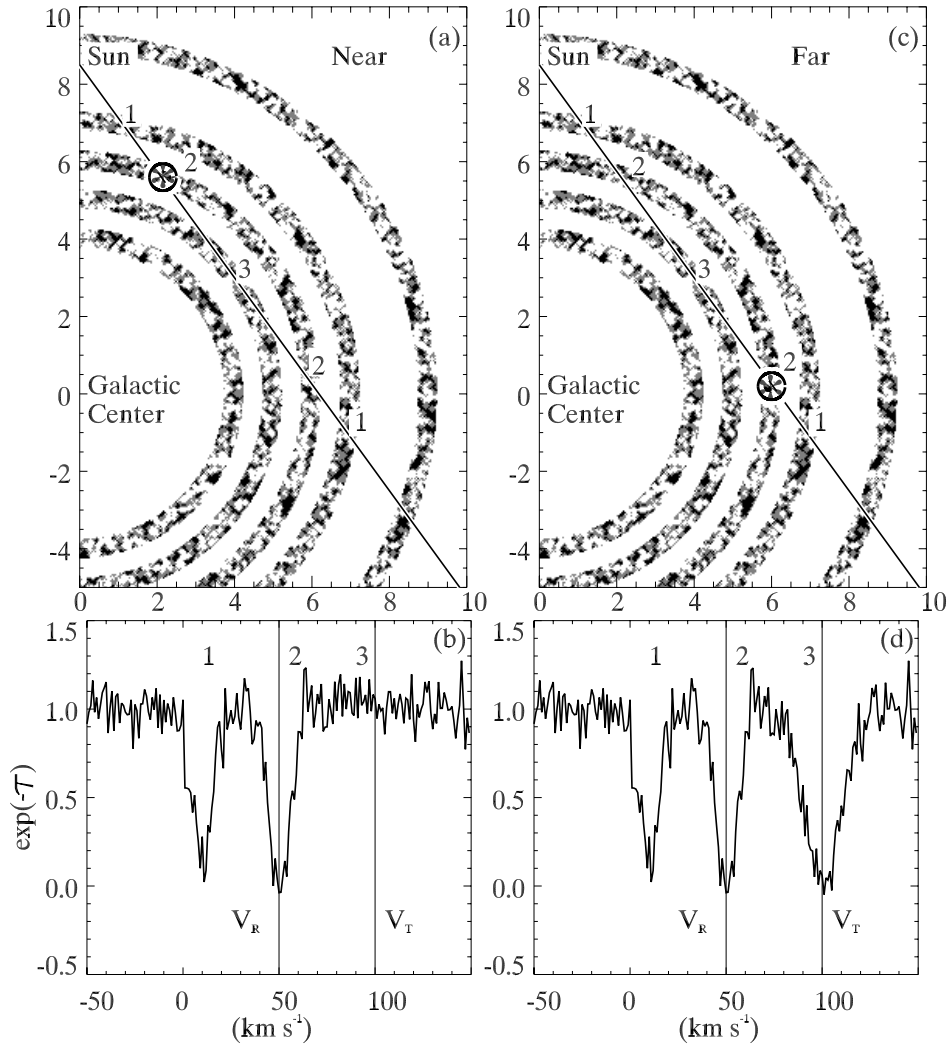


FIG. 1.—Face-on schematic diagrams of the Galaxy for (a) near and (c) far kinematic distance. The numbered ticks mark distances in kiloparsecs from the Galactic center. Panels b and d show the schematic spectra corresponding to the sight lines indicated in panels a and c, respectively.

Schematic absorption spectra for the indicated lines of sight are shown in Figures 1b and 1d. The vertical axis of the spectra represents the expected line-to-continuum intensity ratio, which is equivalent to  $\exp(-\tau_{\text{line}})$ . The radial velocities of the H I clouds that are numbered along the lines of sight are also indicated in the spectra. The recombination-line velocity  $V_r$  of the H II region complex in Figure 1 is  $50 \text{ km s}^{-1}$ , and the tangent-point velocity  $V_t$  for this line of sight is  $100 \text{ km s}^{-1}$ . Both velocities are marked with vertical lines in the schematic absorption spectra. The recombination-line velocity corresponds to two possible kinematic distances, both at a Galactocentric radius of 6 kpc (throughout this paper, we assume that  $R_0 = 8.5 \text{ kpc}$ ). The maximum velocity of absorption is used to discriminate between sources at the near and far kinematic distances. If the absorption spectrum toward the H II region resembles the spectrum on the left-hand side, then we assign it to the near kinematic distance, and if it resembles the spectrum on the right-hand side, we assign it to the far kinematic distance.

Resolution of the KDA for H II regions dramatically reduces the uncertainty in their distances. The far kinematic distances for many Galactic H II regions are more than twice as large as their near kinematic distances. Once the KDA is

resolved, the exact values of the assigned kinematic distances depend somewhat on the rotation curve model used to calculate them, but the results of various rotation curves typically agree to within 5% or 10%. Similarly, the detailed shape and location of any Galactic structures (e.g., spiral arms) identified using kinematic distances depend on the rotation curve employed to compute the distances. We demonstrate below in § 3.3, however, that the overall placement and shape of large-scale Galactic features are relatively insensitive to the adopted rotation curve.

## 1.2. Previous Work

The technique of employing absorption studies to resolve the KDA was first used by Wilson (1972), who measured absorption in the  $1_{11} \rightarrow 1_{10}$  transition of formaldehyde toward 73 discrete radio continuum peaks in the Galactic plane. Among these sources, 49 are H II regions with known recombination-line velocities; Wilson detected formaldehyde absorption toward 45. For 28 of the 45 H II regions, he successfully employed the formaldehyde absorption measurements to resolve the KDA and determine unique kinematic distances.

Formaldehyde traces molecular rather than atomic gas. Because the filling factor of molecular gas in the inner Galaxy is much smaller than that of atomic gas, the line of sight to many continuum sources may contain too few molecular absorbers for this technique to be reliable. Specifically, if there is no formaldehyde near the tangent point, the absorption spectrum toward a radio continuum source at the far kinematic distance will not reveal absorption at tangent-point velocities. This lack of high-velocity absorption could lead to an incorrect assignment of the near kinematic distance. The ubiquity of H I clouds makes them a more reliable absorber to use for this method.

Statistical studies of 21 cm H I absorption features have established the frequency distribution of H I absorption features as a function of peak optical depth. For example, Payne, Salpeter, & Terzian (1983) find that the probability of finding an H I absorption dip with a peak optical depth greater than 0.1 along a line of sight, reduced to  $|b| = 90^\circ$ , is between 0.75 and 1.5. Assuming a vertical scale height of 100 pc for the absorbing H I clouds (Kulkarni & Heiles 1987), this probability range implies that the mean free path between cold H I clouds with a peak 21 cm optical depth greater than 0.1 is between 65 and 130 pc. Radio continuum radiation from most H II regions in the inner Galaxy should therefore pass through many H I clouds on its way to the observer. Kuchar & Bania (1994, hereafter KB94) resolved the KDA and determined kinematic distances to 70 H II regions in the first Galactic quadrant using the Arecibo telescope to measure their 21 cm H I absorption spectra. They also made a face-on map of the Galactic distribution of these 70 H II regions and found concentrations of H II regions coincident with the 5 kpc molecular ring and the Sagittarius and Perseus spiral arms.

### 1.3. Initial Sample Selection

In this paper we present the results of a survey at 21 cm using the Very Large Array (VLA), and we use these data to resolve the KDA for 49 compact H II region complexes. Our source selection criteria were chosen to select Galactic embedded star-forming regions. We matched the spatial coverage of our survey to that of the Boston University–Five College Radio Astronomy Observatory Galactic Ring Survey (BU-FCRAO GRS; Simon et al. 2001):  $l = 18^\circ\text{--}52^\circ$  and  $b = \pm 0.5^\circ$ . The GRS is a new survey of  $J = 1 \rightarrow 0$  emission of  $^{13}\text{CO}$  from molecular clouds in the 5 kpc Galactic ring.

We compiled an initial list of target fields centered on sources from the NRAO VLA Sky Survey (NVSS) point-source catalog. The NVSS is an all-sky 20 cm radio continuum survey made with the VLA in the D array (Condon et al. 1998). We selected all NVSS sources in our survey region having 20 cm continuum fluxes greater than 0.4 Jy and angular sizes smaller than  $10'$ .

From this sample, we then selected only those continuum sources that were within  $15''$  of an *IRAS* point source. The thermal component of Galactic radio continuum emission is strongly correlated with far-infrared emission (e.g., Broadbent, Haslam, & Osborne 1989). By choosing only those radio continuum sources coincident with far-infrared point sources, we eliminated most nonthermal radio sources and selected dusty embedded thermal sources, which are most likely to be Galactic. A total of 28 sources met our criteria, and we refer to these 28 continuum sources as the tar-

get list. Each of our 28 observed fields is centered on a target list source.

All but one of the target list sources are within  $3'$  of a radio recombination-line source listed in the catalog of Lockman (1989, hereafter L89). The beam FWHM of the L89 survey is  $3'$ . The presence of recombination-line emission ensures that these sources are H II regions and confirms that our selection criteria have isolated thermal Galactic sources.

### 1.4. Advantages of Interferometry

For measuring 21 cm H I absorption toward Galactic radio continuum sources, the VLA has two important advantages over single-dish instruments. First, extracting absorption spectra from single-dish observations of H I absorption in the Galactic plane usually requires subtraction of the background large-scale diffuse H I emission (Dickey & Lockman 1990). KB94 accomplished this subtraction by averaging the signal from several positions removed from the continuum source by the half-power beam width and subtracting that average from the signal measured directly on the continuum source.

This method relies on the assumption that the background H I emission varies smoothly over the source region. If there are strong gradients in the background over this region, subtraction of the emission will produce significant uncertainty in the measurement of the absorption spectrum. The uncertainty introduced by this subtraction is the dominant source of uncertainty in single-dish H I absorption spectra (Dickey & Lockman 1990).

This source of uncertainty is greatly reduced by using an interferometer. Because interferometers have a minimum baseline length, they effectively filter out spatial frequencies smaller than a threshold value. The minimum baseline length for the C-array configuration of the VLA is 35 m, and in the *L* band, this corresponds to a maximum size of roughly  $10'$  for snapshot observations. Because our observations are relatively insensitive to H I emission on angular scale sizes larger than this, we measure the 21 cm H I absorption spectra directly, without subtracting the H I emission background.

Second, the VLA in the C array provides a higher angular resolution than single-dish instruments. For example, even though the collecting area of Arecibo is more than 5 times that of the VLA, the FWHM of Arecibo's beam at 21 cm is  $4'$ ; almost 20 times that of the VLA in the C array. The effects of beam dilution on compact radio sources are therefore greatly reduced by using the VLA.

Our observations and data reduction are described in § 2. In § 3 we describe our method of discriminating between the near and far kinematic distances and present our main results: a table of distances to 49 H II region complexes and a face-on Galactic representation of their distribution. A discussion of the main sources of uncertainty in our distance measurements is also included in this section. In § 4 we compare our distance determinations with previous measurements. We also examine the correlation between large-scale molecular gas features and the distribution of H II region complexes. Finally, we discuss the asymmetry between the number of near and far H II region complexes. In § 5 we present a summary of the main results and conclusions.

## 2. OBSERVATIONS AND DATA REDUCTION

### 2.1. VLA Observations

The data presented here were collected in 2000 March and April using the NRAO VLA in the C-array configuration in the L band. The correlator was configured to have a total bandwidth of 1.6 MHz, 128 channels, and 12.2 kHz channel<sup>-1</sup>, corresponding to a velocity resolution of 2.6 km s<sup>-1</sup> channel<sup>-1</sup>. Both circular polarizations were observed simultaneously; on-line Hanning smoothing was not implemented. The FWHM of the synthesized beam was 16", which yielded a beam size of 289 arcsec<sup>2</sup> and a gain of 2.37 K mJy<sup>-1</sup>. We used standard flux and bandpass calibrators and selected phase calibrators from the VLA calibrator manual. We observed 28 fields, each centered on a bright Galactic radio continuum source from the target list. The total integration time for each field was typically 10–15 minutes, and spectra typically had rms fluctuations of 15 mJy beam<sup>-1</sup>. To compensate for the limited *u-v* coverage provided by such short snapshots, we observed each field in a mosaic of four pointings, typically spread evenly over 8 hr. One pointing was centered on the radio continuum source, and the other three were each offset by 10' from the source (to the south, northeast, and northwest), forming an equilateral triangle with the radio continuum source at the center.

### 2.2. Data Reduction

We edited and calibrated the data using the standard AIPS software package. Mosaicked dirty image cubes were created from the calibrated *u-v* data using MIRIAD (Sault, Teuben, & Wright 1995). Continuum maps were created by averaging line-free channels (typically a total of 50 channels). The continuum maps were then deconvolved using the MIRIAD task MOSSDI, which implements the SDI CLEAN algorithm (Steer, Dewdney, & Ito 1984). Finally, these CLEAN models were convolved with the CLEAN beams, and the deconvolution residuals were added. These maps were used to measure the positions and fluxes of continuum sources.

We detected 146 serendipitous continuum sources in our 28 target source fields. We used images from the NVSS survey to confirm the reality of all our continuum source detections. These images were obtained through SkyView (McGlynn, Scolick, & White 1996). We extracted 21 cm H I spectra for all sources in our continuum maps that were coincident with obvious peaks in the NVSS maps. Nine of the 146 serendipitous peaks that we identified in the continuum maps do not have NVSS counterparts. These nine sources are probably noise artifacts, and we rejected them from further analysis.

Our attempt to CLEAN the spectral-line data was unsuccessful. Although the VLA in the C array filters out Galactic H I emission on scales larger than 10', it is still sensitive to low-level Galactic H I emission features smaller than 10'. The presence of these emission features confused the CLEAN algorithm and resulted in the introduction of spurious absorption features. We therefore extracted absorption spectra directly from the dirty image cubes. We obtained average H I spectra toward the continuum sources by spatially averaging the brightest contiguous pixels of the dirty image cubes, typically covering an area of 200–300 arcsec<sup>2</sup>. The continuum flux level for each source was measured by fitting a first-order baseline to the average spectrum.

H I absorption dips that were at least 3 times deeper than the standard deviation of baseline fluctuations,  $\sigma$ , were detected toward a total of 158 sources. These 158 sources comprise the absorption detection sample.

## 3. ANALYSIS AND RESULTS

### 3.1. Post Facto Sample Selection

In order to select only H II regions for further analysis, we pruned the absorption detection sample using two post facto selection criteria. First, we correlated our absorption detection sample with the radio recombination-line catalog of L89 and selected only the absorption detection sources within 3' of an H II region listed by L89, resulting in 100 sources.

Although this selection should have removed most non-thermal sources, some extragalactic sources that happened to be within 3' of an L89 H II region could still have contaminated the sample. In order to avoid these extragalactic sources, we excluded 21 sources for which there was significant 21 cm H I absorption present at negative velocities. Absorption features at negative velocities are caused by gas beyond the solar circle, and most radio continuum sources behind this outer Galaxy gas are likely to be extragalactic. Specifically, we excluded a source if at least two consecutive channels with velocities redward of  $-10$  km s<sup>-1</sup> showed 21 cm absorption with an optical depth of 0.4 or greater (our technique for measuring the optical depth of 21 cm absorption is described in a previous paper [Kolpak et al. 2002]). After removing the sources with negative velocity absorption, 79 sources remained. These 79 sources form our H II region list.

At 16" resolution, some large H II region complexes are resolved into several small components (e.g., W49A). In fact, the 79 sources on our H II region list belong to a total of only 51 separate complexes. The components of each complex are all within 3' of the same L89 recombination-line source, i.e., nearly within the L89 survey beam. Hereafter, we refer to each H II region complex by the Galactic coordinates of its brightest component (e.g., G18.149–0.283). Within each complex, the spectra for the individual components are very similar (with the exception of source G25.397–0.141, to be discussed below). These 51 complexes are our H II region complex list.

Our 28 target list sources are a flux-limited sample, but the 51 sources in our H II region complex list are not. Roughly half of these H II region complexes are serendipitous detections with fluxes less than the 0.4 Jy limit chosen for the initially targeted sample. The H II region complex sample is not complete for fluxes below 0.4 Jy.

### 3.2. Resolving the KDA

For most of the 51 sources in the H II region complex list, the recombination-line velocity corresponds to two kinematic distances. The goal of our analysis was to break this ambiguity and select a single kinematic distance for each H II region complex. We accomplished this for each source by measuring the maximum velocity of 21 cm H I absorption and comparing it with the tangent-point velocity  $V_t$  and the recombination-line velocity  $V_r$ . We also evaluated the quality of each distance determination to indicate our level of confidence in the resolution of the KDA for each H II region complex.

The first step was to calculate the two possible kinematic distances for each of the 51 H II region complexes using the radial velocities  $V_r$  reported in the L89 recombination-line catalog (the typical uncertainty in  $V_r$  listed by L89 is  $\pm 2$  km  $s^{-1}$ ). We assumed the C85 rotation curve (with  $R_0 = 8.5$  kpc,  $V_0 = 220$  km  $s^{-1}$ ) to compute these distances.

Then we analyzed the spectrum of each H II region complex to determine which spectral channels show reliable 21 cm H I absorption. We first measured the standard deviation of the noise in the baseline of the averaged spectrum,  $\sigma$ . Then we measured the excursion below the baseline in each channel. As mentioned above, we required this excursion to be at least  $3\sigma$ . To avoid interpreting noise spikes and bad channels as absorption features, we further required that absorption be detected in at least two contiguous channels (over a velocity width of at least 5.2 km  $s^{-1}$ ). The maximum velocity at which we reliably detected 21 cm H I absorption,  $V_a$ , was then used to resolve the KDA.

We assigned near, far, or tangent-point kinematic distance designations for each source by calculating the velocity differences  $V_t - V_r$  and  $V_t - V_a$ . The C85 rotation curve was used to compute  $V_t$  for each line of sight. We found that there are two distinct groups of sources for which  $V_t - V_r > 0$ . One group has  $V_t - V_a$  near 0 and is therefore at the far kinematic distance. The other group has  $V_t - V_a$  significantly greater than 0 and is therefore at the near kinematic distance. Any source with  $V_t - V_r < 0$  must be very near the tangent point.

### 3.2.1. Simulation of KDA Resolutions

Identification of these three groups of sources is not, by itself, sufficient to assign a kinematic distance and a quality to all the H II region complexes. Some sources are near the boundaries between groups, and it is not obvious to which kinematic distance they should be assigned. In addition, it is important to have an estimate of the certainty with which each source can be assigned to one of the groups.

In order to address these issues, we performed a simple simulation. The goal of this simulation was to estimate ranges of  $V_t - V_r$  and  $V_t - V_a$  that correspond to high-quality KDA resolutions. We created a sample of 10,000 randomly placed H II regions with Galactocentric radii between 3 and 8 kpc and Galactic longitudes between  $18^\circ$  and  $50^\circ$ . Our observed H II region complexes were not distributed uniformly in Galactocentric radius. The number of observed H II region complexes between  $R = 4$  and 5 kpc and between 6 and 7 kpc was roughly twice as large as the number between 5 and 6 kpc and 4 times larger than the number inward of 4 kpc and outward of 7 kpc. We designed our simulated H II region population to match this observed Galactocentric radial distribution.

We assigned a circular velocity to each simulated H II region based on the C85 rotation curve. The measured distribution of H II region velocities deviates from purely circular rotation, and this deviation typically has both random and systematic components (e.g., Brand & Blitz 1993). The random component is caused by cloud-cloud dispersion, and the systematic component is often explained as streaming motions along spiral arms. To include the effects of cloud-cloud dispersion, we added a random component to the circular velocity of our simulated H II regions. This random component follows a Gaussian distribution with a mean of 0 km  $s^{-1}$  and a dispersion of 5 km  $s^{-1}$ , which is con-

sistent with published measurements of the cloud-cloud dispersion (e.g., Blitz, Fich, & Stark 1980; Liszt & Burton 1983; C85).

We included streaming motions by adding 10 km  $s^{-1}$  (in the direction of Galactic rotation) to the circular velocities of 50% (randomly selected) of the simulated H II regions between Galactocentric radii of 4.5 and 5.5 kpc and between 6 and 7 kpc. These Galactocentric radii correspond to the locations of the 5 kpc molecular ring and the Sagittarius spiral arm. It is also at these Galactocentric radii that some H II region complexes from our observed sample have recombination-line velocities up to 20 km  $s^{-1}$  larger than the tangent-point velocity. Such large deviations from circular rotation at particular Galactocentric radii are probably due to large-scale streaming motions. We chose the sign and size of the streaming motion in order to match the distribution of observed H II region velocity differences.

Our next task was to simulate the observed quantities  $V_r$  and  $V_a$ . We constructed  $V_r$  by calculating the radial velocity component for each simulated H II region and subtracting the radial component of the Galactic orbital motion of the Sun. Because of the ubiquity of absorbing H I clouds, we calculated  $V_a$  assuming that absorption would be detected at all velocities, up to the largest relative radial velocity along the line of sight to the simulated H II region. Therefore, for sources on the near side of the locus of tangent points,  $V_a$  is equal to  $V_r$ , and for sources on the far side of the locus of tangent points,  $V_a$  is equal to  $V_t$ .

We also included streaming motions in our calculation of  $V_a$ . For H II regions nearer than the tangent point, the 21 cm absorption near  $V_a$  is caused by gas that is very close to the H II region. If the H II region is participating in a streaming motion (i.e., if its circular velocity has been raised by 10 km  $s^{-1}$ ), then the nearby H I cloud is probably participating in the same streaming motion and is therefore moving at a velocity comparable to the recombination-line velocity of the H II region. For near-side H II regions that had  $V_r$  augmented by streaming motions, we added a 10 km  $s^{-1}$  streaming motion to  $V_a$  as well. This procedure is supported by the fact that for all but two of our observed sources, we measure 21 cm absorption at the recombination-line velocity of the H II region.

For H II regions beyond the tangent point, the highest velocity absorption comes from H I near the tangent point. If this tangent-point gas is participating in a streaming motion, then  $V_a$  for these sources will be augmented. We therefore added 10 km  $s^{-1}$  to  $V_a$  for 50% (randomly selected) of the far-side H II regions for which the Galactocentric radius of the tangent point was between 4.5 and 5.5 kpc or between 6 and 7 kpc.

Finally, we added a Gaussian-distributed random velocity to  $V_a$  for all the simulated H II regions to simulate cloud-cloud motions in the absorbing H I gas. This random component had a mean of 0 km  $s^{-1}$  and a dispersion of 5 km  $s^{-1}$ .

Figure 2 shows the plot of velocity differences for the simulated H II region sample. We analyzed the distribution of sources by first binning the points into cells of  $3 \times 3$  (km  $s^{-1}$ )<sup>2</sup>. We then computed the fractions of points in each cell corresponding to sources on the near and far sides of the locus of tangent points. The contour line in the top right portion of the plot encloses a region in which all cells contain at least 90% near sources, and the contour in the bottom right portion of the plot encloses a region in which all cells contain at least 90% far sources.

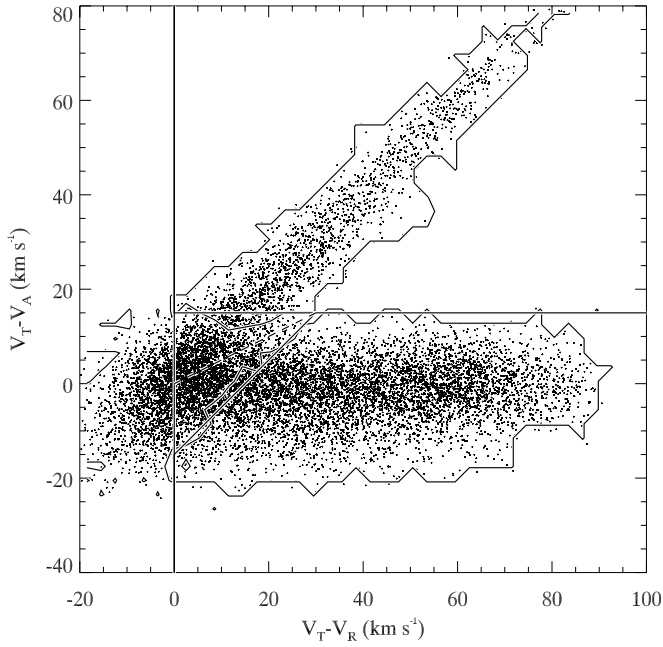


FIG. 2.—Velocity differences for the simulated H II region complexes. The vertical axis represents the difference between the tangent-point velocity and the maximum velocity at which we measured absorption,  $V_t - V_a$ . The horizontal axis represents the difference between the tangent-point velocity and the recombination-line velocity,  $V_t - V_r$ . The irregularly shaped contours enclose regions where locally at least 90% of the simulated H II regions are at the near (*top right contour*) or far (*bottom right contour*) kinematic distance. The straight solid lines mark approximations to these contours. Above the dashed line, at least 50% of the simulated H II regions are at the near kinematic distance, while below the dashed line, at least 50% are at the far kinematic distance.

The straight, solid lines mark approximations to these boundaries. All sources in the top right portion of the plot can be assigned to the near kinematic distance with a high degree of confidence, and those in the bottom right portion can be confidently assigned to the far kinematic distance. The triangle near the center of the plot marks a zone of higher uncertainty. The results of our simulation indicate that H II region complexes that fall inside this region have a significant chance of being at either of the near or far kinematic distances. The dashed, diagonal line divides this region into two pieces. Above the dashed line, greater than 50% of the simulated H II regions in each cell are at the near kinematic distance, while below the dashed line, greater than 50% are at the far kinematic distance.

### 3.2.2. KDA Resolutions

These solid and dashed lines are also drawn in Figure 3, which is a plot of  $V_t - V_a$  against  $V_t - V_r$  for our observed H II regions. We used the zones delineated by these lines to resolve the KDA. We assigned all observed H II region complexes in the bottom right region of the plot to the far kinematic distance, and those in the top right region to the near kinematic distance. Based on our simulation, we have a high level of confidence in these KDA resolutions, and we assign them a quality of “A.” Within the triangular region near the center of the plot, we assign all sources above the dashed line to the near kinematic distance and those below the line to the far kinematic distance. Because these KDA resolutions are more uncertain, we assign them a quality of “B.”

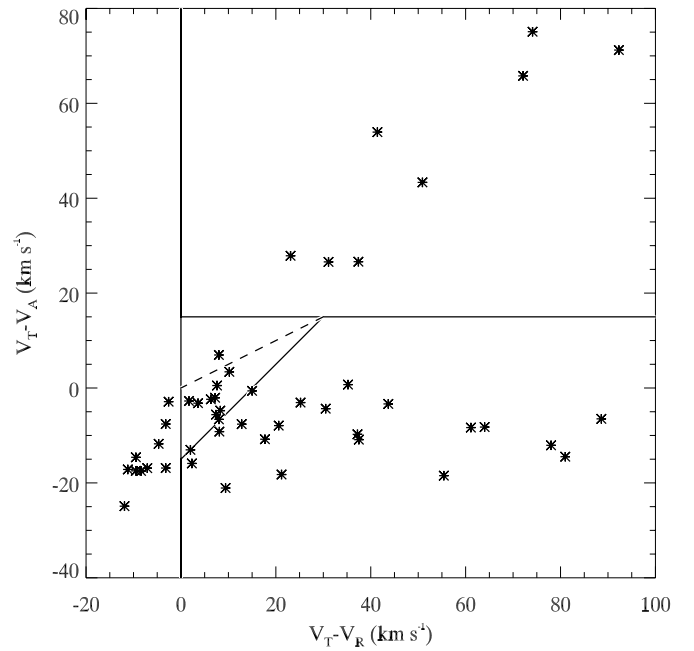


FIG. 3.—Velocity differences plot of the 49 H II region complexes for which we resolved the KDA. The solid and dashed lines are the same as in Fig. 2. The sources outside of the triangular region near the center of the plot represent our quality A kinematic distance determinations, and those sources within the triangle represent our quality B determinations.

The left side of the plot contains H II region complexes with recombination-line velocities greater than the tangent-point velocity. We therefore assign these sources to the tangent-point distance with a quality of A.

Using this technique, we resolved the KDA and determined unique kinematic distances for all but two (see note on G23.900+0.068 and G31.243–0.110 below) of the 51 H II region complexes.

In order to probe the importance of our choice of rotation curve, we calculated the kinematic distances to these 49 H II region complexes again, using the rotation curve of Olling & Merrifield (1998, hereafter OM98). Because their best-fit curve (for  $R_0 = 7.1$  kpc,  $\theta_0 = 184$  km s $^{-1}$ ) is not given in analytic form, we estimated its form from their Figure 1 (*bottom left panel*). We represent this as a two-part linear curve:

$$\theta_0 = \begin{cases} 155 + 10R, & 2.9 \leq R < 3.5, \\ 195.3 - 1.5R, & 3.5 \leq R < 19.4. \end{cases} \quad (1)$$

Here,  $R$  represents the Galactocentric radius in kiloparsecs, and  $\theta$  is the circular rotation speed in km s $^{-1}$ . Because the OM98 rotation curve adopts a value of  $R_0 = 7.1$  kpc, we rescaled the kinematic distances to  $R_0 = 8.5$  before comparing them with the results from the C85 rotation curve.

### 3.3. Results

Figures 4a and 5 show H I absorption spectra for 12 representative sources from our H II region complex list. Absorption spectra for the remaining 37 H II region complexes for which we were able to resolve the KDA are published as Figures 4b–4h in the electronic version of this paper, which is available from the *Astrophysical Journal* Web site. The maximum velocity of reliably detected 21 cm absorption  $V_a$ , the

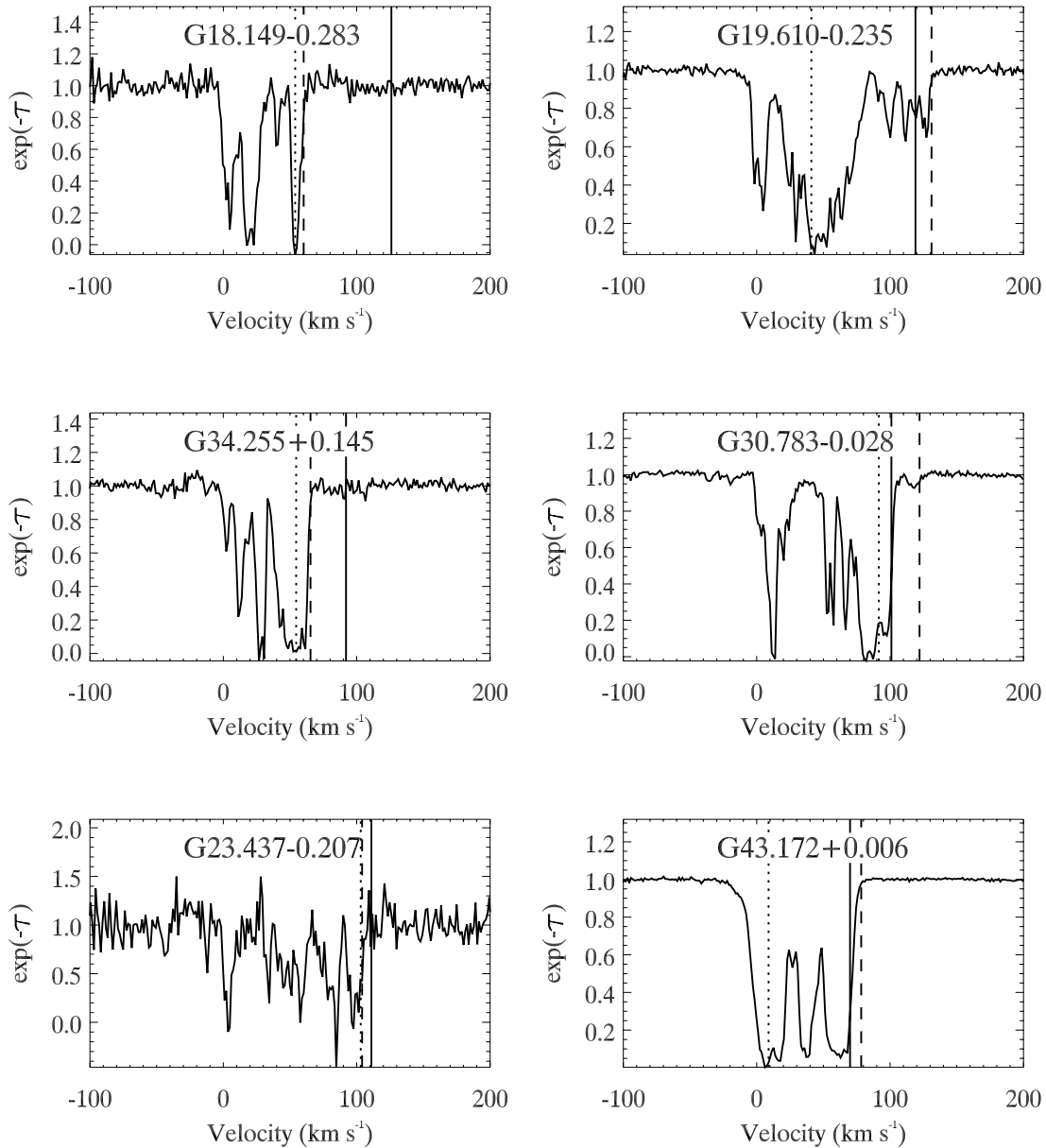


FIG. 4a

FIG. 4.—(a) Example H I absorption spectra for six of the 49 sources on the H II region complex list. The name of each source is at the top of each panel. The tangent-point velocity  $V_t$  is marked by a solid vertical line, and the recombination-line velocity  $V_r$  is marked by a dotted vertical line. The dashed line marks the maximum velocity at which we measured H I absorption,  $V_a$ . The vertical axis of the spectra represents the observed line-to-continuum intensity, which is equivalent to  $\exp(-\tau_{\text{line}})$ . We resolved the KDA by comparing this maximum velocity of H I absorption with the source and tangent-point velocities. Sources shown on the left are complexes that we assigned to the near kinematic distance. The sources at the top left and middle left have a quality of A, and the source at bottom left has a quality of B. We assigned the sources shown on the right to the far kinematic distance with qualities of A. See the electronic edition of the *Astrophysical Journal* for additional H I absorption spectra.

tangent-point velocity  $V_t$ , and the recombination-line velocity  $V_r$  are indicated in each spectrum.

Table 1 lists important parameters for the 51 sources of our H II region complex sample. Column (1) contains the source names. Two sources, G23.900+0.068 and G31.243–0.110, are listed twice because L89 reports two recombination-line velocity components toward each of these sources. Columns (2) and (3) list the right ascension and declination (J2000.0) for the peak pixel value for each source as determined from our continuum maps. Columns (4)–(6) contain the H II region complex recombination-line velocity, tangent-point velocity, and the maximum velocity of H I absorption for each source. Column (7) lists our

determination of whether the sources are at the near kinematic distance (N), the far kinematic distance (F), the tangent point (T), or undetermined (?), and column (8) contains our kinematic distance for each source along with an estimate of the uncertainty in the distance. Column (9) lists the quality assignment (A or B) for our resolution of the KDA for each H II region complex.

Of the 51 sources, we determined that nine are at the near kinematic distance, 28 are at the far kinematic distance, and 12 are at the tangent-point distance. The distances to the other two sources remain undetermined, as explained below. One H II region complex at the near kinematic distance and eight at the far kinematic distance received a qual-

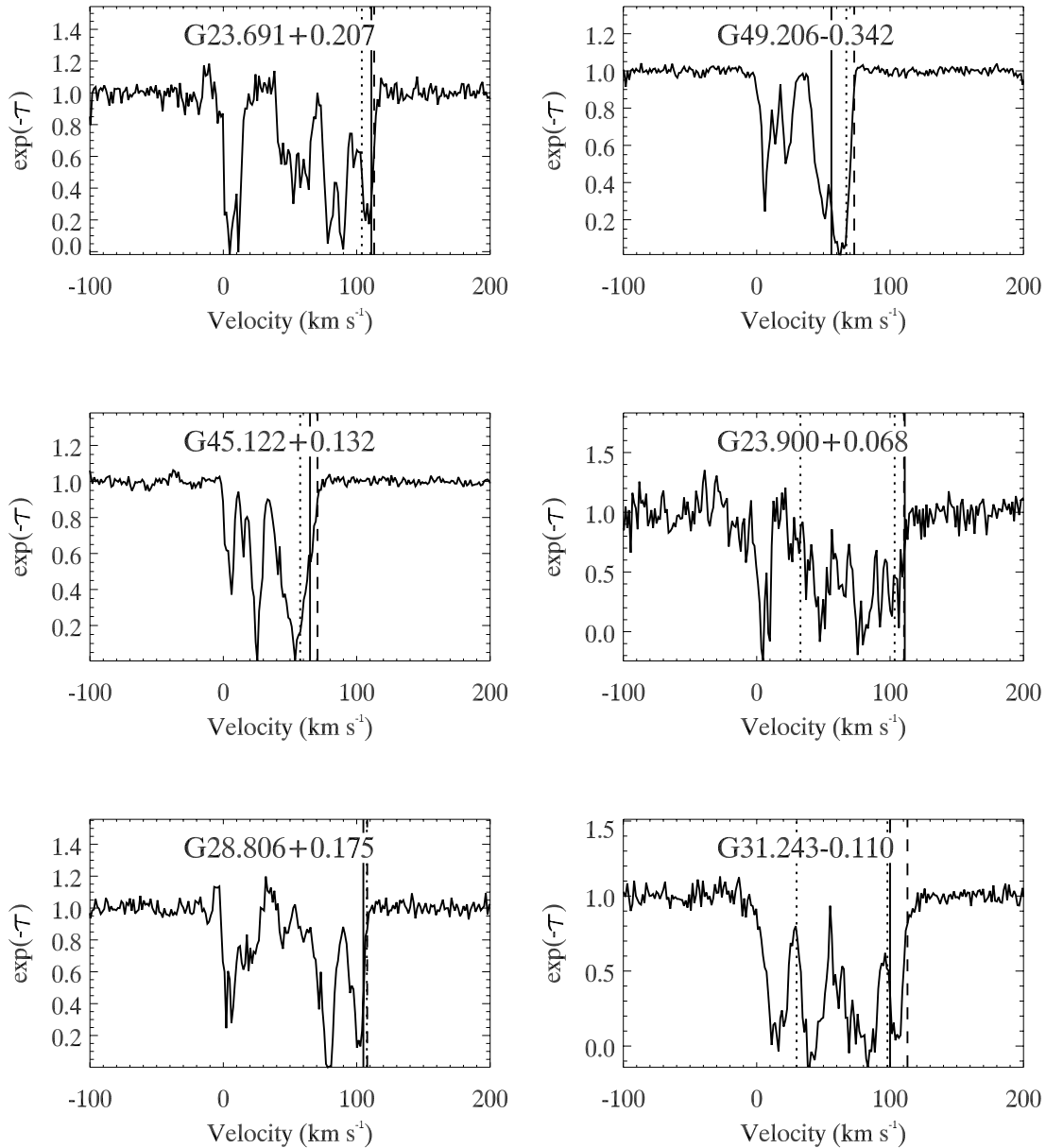


FIG. 5.—Six more examples of H I absorption spectra of H II region complexes. The spectra are displayed as in Fig. 4, although two recombination-line velocities are indicated for both G23.900+0.068 and G31.243–0.110. We assign the sources shown at bottom left and at top, middle, and bottom right to the tangent-point velocity. The sources at bottom left and top right have a quality of A, and the sources at middle right and bottom right have a quality of B.

ity of B because they fall within the triangular region in Figure 3. We also assigned a quality of B to two H II region complexes at the tangent-point distance for reasons that are explained in § 4.1.1. The remaining 38 H II region complexes received a quality of A.

The distances listed in Table 1 are based on the C85 model of circular Galactic rotation. Perturbations to circular rotation caused by random gas motions and spiral-arm streaming motions typically have an amplitude of 5–10 km s<sup>−1</sup> (Bania & Lockman 1984). Using the C85 rotation curve to compute distances therefore introduces an uncertainty, because the rotation curve does not account for these motions. The uncertainties in distance listed in column (8) are calculated by allowing a ±5 km s<sup>−1</sup> range in velocity centered on the recombination-line velocity of each H II region

complex. We then use the C85 rotation curve to compute the distances corresponding to the high and low ends of this velocity range. We list the resulting full range in distance as a distance uncertainty.

For most of the H II regions, the uncertainty is typically 10%–15% of the distance. Near the tangent point, the distance depends very strongly on the velocity, and the uncertainties are larger, sometimes as high as ±1 kpc. Some tangent-point H II region complexes have recombination-line velocities greater than 5 km s<sup>−1</sup> above the tangent-point velocity. Because their radial velocities are greater than the tangent-point velocity, these sources are probably quite close to the tangent point. Moreover, calculation of distance uncertainties for these H II region complexes based on recombination-line velocity ranges of ±5 km s<sup>−1</sup> is not

TABLE 1  
H II REGION COMPLEXES

Source Name (1)	R.A. (J2000.0) (2)	Decl. (J2000.0) (3)	$V_r$ (km s <sup>-1</sup> ) (4)	$V_l$ (km s <sup>-1</sup> ) (5)	$V_a$ (km s <sup>-1</sup> ) (6)	KDA Resolution (7)	Distance (kpc) (8)	Quality Assignment (9)
G18.149-0.283.....	18 25 01.2	-13 15 28.9	53.9	126	60	N	4.3 ± 0.2	A
G18.259-0.307.....	18 25 19.1	-13 10 19.1	50.9	125	50	N	4.1 ± 0.3	A
G18.303-0.390 <sup>a</sup> .....	18 25 42.2	-13 10 18.5	32.7	125	54	N	3.0 ± 0.4	A
G19.610-0.235 <sup>a</sup> .....	18 27 38.3	-11 56 35.4	41.0	119	131	F	12.6 ± 0.3	A
G19.678-0.132.....	18 27 23.7	-11 50 06.2	55.0	119	127	F	11.8 ± 0.2	A
G21.874+0.007 <sup>a</sup> .....	18 31 02.6	-09 49 31.2	24.4	113	119	F	13.7 ± 0.4	A
G23.437-0.207.....	18 34 44.2	-08 32 15.5	103.0	111	104	N	6.6 ± 0.5	B
G23.691+0.207 <sup>a</sup> .....	18 33 43.4	-08 07 17.1	103.8	111	113	F	8.9 ± 0.5	B
G23.871-0.120 <sup>a</sup> .....	18 35 13.9	-08 06 44.3	73.8	111	121	F	10.7 ± 0.2	A
G23.900+0.068.....	18 34 36.7	-08 00 00.0	32.8	111	110	?	...	...
G23.900+0.068.....	18 34 36.7	-08 00 00.0	103.4	111	110	T	7.7 ± 1.1	B
G23.955+0.150 <sup>a</sup> .....	18 34 25.2	-07 54 48.3	78.9	110	83	N	5.1 ± 0.2	A
G24.129-0.070.....	18 35 31.9	-07 51 36.9	86.9	110	82	N	5.5 ± 0.3	A
G24.469+0.491 <sup>a</sup> .....	18 34 09.3	-07 18 00.4	99.8	110	107	F	9.2 ± 0.4	B
G25.380-0.181 <sup>a</sup> .....	18 38 14.9	-06 48 00.5	59.1	110	67	N	4.0 ± 0.3	A
G25.404-0.253.....	18 38 33.0	-06 48 42.6	67.6	110	55	N	4.5 ± 0.3	A
G26.544+0.413 <sup>a</sup> .....	18 38 16.4	-05 29 36.1	88.4	109	117	F	9.7 ± 0.3	A
G28.652+0.027.....	18 43 31.4	-03 47 45.6	102.4	106	109	F	8.2 ± 0.6	B
G28.806+0.175 <sup>a</sup> .....	18 43 16.7	-03 35 29.0	107.6	105	108	T	7.4 ± 0.7	A
G29.957-0.018 <sup>a</sup> .....	18 46 04.3	-02 39 20.2	96.7	103	105	F	8.4 ± 0.5	B
G30.535+0.021 <sup>a</sup> .....	18 46 59.4	-02 07 24.7	45.6	101	119	F	11.6 ± 0.3	A
G30.783-0.028.....	18 47 37.0	-01 55 30.7	91.6	101	122	F	8.7 ± 0.5	A
G31.243-0.110 <sup>a</sup> .....	18 48 44.9	-01 33 11.7	29.9	100	113	?	...	...
G31.243-0.110 <sup>a</sup> .....	18 48 44.9	-01 33 11.7	98.0	100	113	T	7.3 ± 0.5	B
G31.279+0.063.....	18 48 11.9	-01 26 32.3	104.7	100	112	T	7.3	A
G31.395-0.259.....	18 49 33.4	-01 29 09.3	86.2	99	107	F	8.9 ± 0.3	A
G31.412+0.308 <sup>a</sup> .....	18 47 34.1	-01 12 43.9	102.2	99	107	T	7.2 ± 0.8	A
G32.799+0.190 <sup>a</sup> .....	18 50 31.1	00 01 54.0	15.0	96	110	F	13.1 ± 0.3	A
G33.915+0.109 <sup>a</sup> .....	18 52 50.6	00 55 28.7	101.4	93	110	T	7.0	A
G34.255+0.145.....	18 53 20.1	01 14 37.1	54.6	92	65	N	3.6 ± 0.3	A
G35.574+0.068 <sup>a</sup> .....	18 56 01.0	02 22 56.2	50.5	88	99	F	10.5 ± 0.3	A
G35.590-0.026.....	18 56 22.9	02 21 13.0	52.8	88	87	F	10.4 ± 0.3	A
G37.360-0.231.....	19 00 21.1	03 50 04.3	40.3	84	87	F	10.9 ± 0.3	A
G37.543-0.112 <sup>a</sup> .....	19 00 15.7	04 03 06.0	52.5	83	87	F	10.0 ± 0.4	A
G37.749-0.109.....	19 00 37.8	04 14 10.5	57.8	83	86	F	9.6 ± 0.4	A
G37.763-0.216.....	19 01 02.2	04 11 59.1	65.3	83	94	F	9.0 ± 0.4	A
G37.872-0.397 <sup>a</sup> .....	19 01 52.9	04 12 49.8	60.8	82	100	F	9.4 ± 0.4	A
G42.434-0.262 <sup>a</sup> .....	19 09 50.2	08 19 39.9	62.7	71	76	F	8.0 ± 0.6	B
G43.172+0.006 <sup>a</sup> .....	19 10 15.2	09 06 22.1	8.9	70	78	F	11.6 ± 0.3	A
G43.186-0.526 <sup>a</sup> .....	19 12 11.3	08 52 21.2	55.0	70	71	F	8.5 ± 0.4	A
G45.122+0.132 <sup>a</sup> .....	19 13 27.9	10 53 34.9	57.6	65	71	F	7.6 ± 0.7	B
G45.455+0.058 <sup>a</sup> .....	19 14 21.7	11 09 13.0	55.9	64	73	F	7.7 ± 0.6	A
G45.478+0.131 <sup>a</sup> .....	19 14 08.5	11 12 28.4	56.0	64	71	F	7.7 ± 0.6	B
G45.824-0.284 <sup>a</sup> .....	19 16 17.8	11 19 16.0	62.3	64	67	F	6.5 ± 0.7	B
G48.929-0.281.....	19 22 15.1	14 03 55.8	66.5	57	74	T	5.6	A
G48.984-0.304.....	19 22 26.5	14 06 11.4	65.5	56	71	T	5.6	A
G49.079-0.374.....	19 22 52.9	14 09 14.1	67.9	56	81	T	5.6	A
G49.206-0.342 <sup>a</sup> .....	19 23 00.8	14 16 51.5	67.2	56	73	T	5.5	A
G49.370-0.302 <sup>a</sup> .....	19 23 11.2	14 26 40.0	53.7	56	72	F	6.3 ± 0.8	A
G49.480-0.386.....	19 23 42.4	14 30 06.1	58.2	55	72	T	5.5 ± 0.8	A
G49.586-0.385.....	19 23 54.7	14 35 44.0	62.1	55	72	T	5.5	A

NOTE.—Units of right ascension are hours, minutes, and seconds, and units of declination are degrees, arcminutes, and arcseconds.

<sup>a</sup> These sources form the initial target list.

possible. Hence, we have included neither distance uncertainties nor error bars for H II region complexes with recombination-line velocities greater than 5 km s<sup>-1</sup> above the tangent-point velocity.

The kinematic distances computed using the OM98 rotation curve are not significantly different from the results of the C85 rotation curve. The average difference is less than

5%, and the difference was greater than 10% for only five of the H II region complexes. Because the results of the two rotation curves are so similar, we do not report the distances computed from the OM98 curve.

In contrast, the average ratio of the far kinematic distance to the near kinematic distance for these 49 H II region complexes is 2.5. Our resolution of the KDA has, therefore, sub-

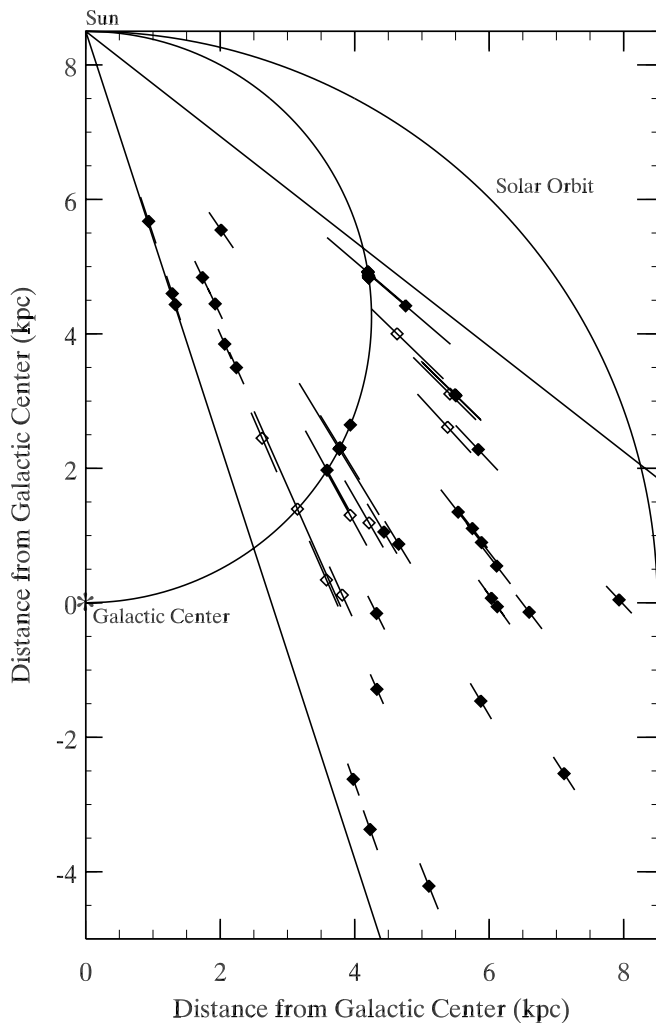


FIG. 6.—Positions of the 49 H II region complexes for which we resolved the KDA, plotted in a face-on representation of the Galaxy. The sources were placed according to their longitude and kinematic distance, and the error bars represent a  $\pm 5 \text{ km s}^{-1}$  variation in the recombination-line velocity (except for G23.900+0.068 and G31.243–0.110; see § 4.1.1). The long, straight lines indicate our longitude range, and the large semicircle is the locus of tangent points that separates near from far sources. Sources with quality A kinematic distance determinations are marked with filled squares, and those with quality B kinematic distance determinations are marked with open squares.

stantially improved the distance estimates for these H II region complexes.

Using the distances and longitudes in Table 1, we constructed a face-on map of the Galactic distribution of the 49 sources from our H II region complex list for which we resolved the KDA. Figure 6 shows this distribution of H II region complexes. The filled squares mark the positions of H II region complexes with a quality of A, and the sources with a quality of B are marked by open squares. The number of sources on the far side of the locus of tangent points exceeds that on the near side by a factor of  $\sim 4$ . The distribution of sources is not random. Distinct concentrations and gaps are evident that resemble segments of rings or spiral arms.

We also produced a face-on map of these 49 H II region complexes using the distances calculated from the OM98 rotation curve. The two face-on diagrams are shown

together in Figure 7 for comparison. Although the exact positions of several H II region complexes differ slightly according to which rotation curve is employed to calculate the distances, the overall pattern of H II region complexes is the same.

#### 4. DISCUSSION

##### 4.1. Notes on Specific Sources

Complications arose while assigning kinematic distances to some sources. Two recombination-line velocity components are listed in L89 for each of three of the sources on our H II region complex list. In another case, we detected two radio continuum peaks separated by only  $2.6''$  with very different absorption spectra. We give the details for each of these difficult cases below.

##### 4.1.1. G23.900+0.068 and G31.243–0.110

Both of these sources are blended H II regions. Their positions are each listed in the L89 recombination-line survey with two velocity components. These two velocity components probably come from two separate H II region complexes along each of these two lines of sight that were blended together in the same beam in the recombination-line observations. Both G23.900+0.068 and G31.243–0.110 have one recombination-line component at a low velocity ( $< 50 \text{ km s}^{-1}$ ) and another at a high velocity ( $90\text{--}100 \text{ km s}^{-1}$ ), slightly less than the tangent-point velocity. Our 21 cm continuum maps for G23.900+0.068 and G31.243–0.110, however, reveal only one compact component at each position. We do not detect two separate components with distinct absorption spectra at either position that could correspond to the two recombination-line velocity components reported for each of these sources.

We measure H I absorption toward both G23.900+0.068 and G31.243–0.110 at velocities up to and including the tangent-point velocity, and therefore, at least one of the H II regions along each of these sight lines must be at least as distant as the tangent point. Because we cannot determine which H II region is responsible for the high-velocity absorption, however, we cannot resolve the KDA for any of these four H II region complexes.

On the other hand, because the *high-velocity* recombination-line component is centered at a velocity nearly as large as the tangent-point velocity for both G23.900+0.068 and G31.243–0.110, the difference between the near and far kinematic distances for these H II region complexes is small ( $\sim 1 \text{ kpc}$ ). We therefore place the high-velocity H II region complexes at the tangent-point distance and include a distance uncertainty equal to the difference between the near and far kinematic distances. We also give these distance determinations a quality of B.

For the low-velocity components, the difference between the near and far kinematic distances is large ( $\sim 10 \text{ kpc}$ ), and it is unreasonable to place them at the tangent-point distance. Because their H I absorption spectra are blended with those of the high-velocity complexes, we are unable to resolve the KDA for these two low-velocity H II region complexes.

##### 4.1.2. G30.535+0.021

Although L89 reports two different recombination-line velocities,  $46.1$  and  $95.2 \text{ km s}^{-1}$ , at the position of this H II

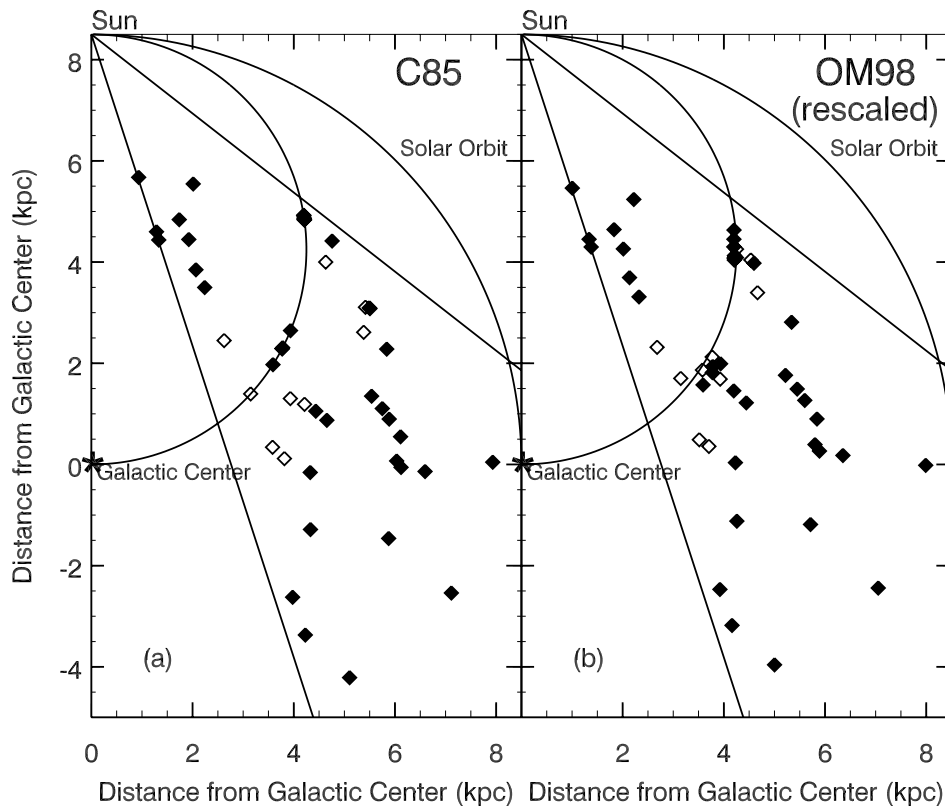


FIG. 7.—(a) Same as Fig. 6. (b) Face-on map of the same 49 H II region complexes with distances calculated using the OM98 rotation curve. The distances have been rescaled so that  $R_0 = 8.5$  kpc. The position and shape of the large-scale features are essentially the same in both plots.

region complex, Wood & Churchwell (1989, hereafter WC89) report a single velocity,  $45.6 \text{ km s}^{-1}$ . The observations of WC89 were made in the H76- $\alpha$  line with the VLA in the D array with a synthesized beam size of  $4''.4$ . They obtained spectra by integrating over roughly one synthesized beam. We obtained our 21 cm H I absorption spectrum for this source over a very similarly sized region, centered at the same position. The second velocity component seen by L89 may originate from a source other than G30.535+0.021. We therefore used the velocity measured by WC89 to compute a kinematic distance for G30.535+0.021.

#### 4.1.3. G25.397–0.141

Source G25.397–0.141 is only  $2/3$  from an L89 recombination-line source, and its spectrum reveals no substantial negative velocity absorption. Nevertheless, we have not included this source on the H II region complex list. The L89 recombination-line source associated with G25.397–0.141 is also only  $0/3$  from another H II region complex, G25.380–0.181. In fact, G25.397–0.141 and G25.380–0.181 are so close that we initially assumed they were a single H II region complex. The spectrum of G25.397–0.141, however, shows 21 cm absorption up to  $100 \text{ km s}^{-1}$ , whereas the maximum velocity of reliably detected absorption in the spectrum of G25.380–0.181 is  $67 \text{ km s}^{-1}$ . This difference suggests that these two sources are separate H II region complexes. The velocity of the nearby recombination-line source is  $59.1 \text{ km s}^{-1}$ , and because source G25.380–0.181 shows no absorption at velocities significantly greater than this, we assign it to the near kinematic distance.

Because G25.397–0.141 shows absorption almost up to the tangent-point velocity of  $110 \text{ km s}^{-1}$ , it is probably at least as distant as the tangent point. Unfortunately, we have no recombination-line velocity to associate with the more distant source, G25.397–0.141, and so we cannot determine a kinematic distance for it.

#### 4.2. Comparison with Previous Determinations

Previous studies have determined distances for many of the 51 H II region complexes in Table 1. A comparison of our KDA resolutions with those derived using different techniques is important for two reasons. First, agreement between our results and previous determinations enhances confidence in the various techniques and KDA resolutions. In addition, by studying the disagreements, we may learn about problems associated with the KDA resolution techniques.

KB94 resolved the KDA for 70 H II region complexes and determined kinematic distances based on the C85 rotation curve. Our determinations match theirs for 25 of 27 common sources.

One of the discrepancies is for G30.535+0.021. In their analysis, KB94 used both of the recombination-line velocity components reported by L89 and treated G30.535+0.021 as two separate H II region complexes. Because L89 lists both a low- and high-velocity component toward G30.535+0.021 and because KB94 measured absorption up to the tangent-point velocity toward this source, they were unable to resolve the KDA for either the low- or the high-velocity H II region complex. As explained in § 4.1.2, we regarded this as a single H II region complex with a recombination-line

velocity of  $45.6 \text{ km s}^{-1}$ . We measured H I absorption beyond the tangent-point velocity, and G30.535+0.021 falls well within the 90% confidence contour for far sources in Figure 3. We therefore assigned the far kinematic distance and a quality of A to this source.

The other discrepancy is for source G30.783–0.028. This source has a recombination-line velocity of  $91.6 \text{ km s}^{-1}$ , and the tangent-point velocity for this line of sight is  $101 \text{ km s}^{-1}$ . In their Table 1, KB94 list  $94.3 \text{ km s}^{-1}$  as the nearest velocity to the recombination-line velocity at which H I absorption was detected for this H II region complex, but the *maximum* velocity at which they detected H I absorption is not listed. Presumably, it is less than the tangent-point velocity, and they therefore assigned the H II region complex to the near kinematic distance, 5.7 kpc. If  $94.3 \text{ km s}^{-1}$  in fact represents the maximum velocity at which KB94 detected H I absorption, they would place this source just above the dashed, diagonal line in Figure 3, and we would assign it a quality B, near kinematic distance. We detected very strong 21 cm H I absorption toward this source beyond the tangent-point velocity (see Fig. 4a [middle right]). G30.783–0.028 therefore falls well below the uncertain triangular zone in Figure 3, and we assign this source to the far kinematic distance with a quality of A.

We also compared our H II region complex distances with the list compiled by Wilson (1980, hereafter W80). Of 36 sources common to both our lists, there are 23 matches and 13 discrepancies. For five of the discrepancies (G19.610–0.235, G19.678–0.132, G30.783–0.028, G31.395–0.259, and G35.590–0.026), we assign the H II region complex to the far distance and Wilson assigns it to the near distance (see Table 2 of W80). All of these H II region complexes fall within the 90% confidence contour for far sources in Figure 3, and so their distance determinations have A qualities. We measure 21 cm absorption at velocities greater than the tangent-point velocity for all but G35.590–0.026. For this source, we only detected H I absorption up to  $87 \text{ km s}^{-1}$ , and the tangent-point velocity is  $88 \text{ km s}^{-1}$ . Because the recombination-line velocity for G35.590–0.026 is only  $52.8 \text{ km s}^{-1}$ , however, this source must be behind a high-velocity H I cloud near the tangent point.

To understand these five discrepancies, it is important to note that the determinations of W80 are based primarily on H<sub>2</sub>CO absorption spectra collected by Downes et al. (1980, hereafter D80). As mentioned in § 1.2, formaldehyde absorption experiments may yield false near determinations because of the small filling factor of molecular gas in the disk, which could lead to a lack of gas at the tangent point along a particular line of sight.

For three additional discrepancies (G23.955+0.150, G25.380–0.181, and G25.404–0.253), we assign the H II region complexes to the near distance and W80 assigns them to the far distance (although the distances for these three sources are listed in Table 2 of W80 with question marks to indicate some uncertainty). These three sources fall well within the 90% confidence contour for near sources. In all three cases, the maximum velocity of H I absorption is at least  $25 \text{ km s}^{-1}$  below the tangent-point velocity. We also do not detect any H I absorption at velocities greater than  $8 \text{ km s}^{-1}$  above the recombination-line velocity of these H II region complexes. Our results do not support the assignment of the far kinematic distance to any of these three sources.

According to the C85 rotation curve, the tangent-point velocity for all three of these sources is  $110 \text{ km s}^{-1}$ . For G23.955+0.150, D80 detected a single formaldehyde absorption feature, centered at  $81.3 \text{ km s}^{-1}$ , with a half-power width of  $3.2 \text{ km s}^{-1}$  (D80 list an uncertainty of 2–5  $\text{km s}^{-1}$  for the line centers and half-power widths), and for G25.404–0.253, D80 did not detect any formaldehyde absorption. Although W80 gives no indication of what other information was used to resolve the KDA for these sources, it seems unlikely that he assigned them to the far kinematic distance based solely on the D80 survey data.

For G25.380–0.181, D80 detected a formaldehyde absorption line at  $95.7 \text{ km s}^{-1}$  with a half-power width of  $3.3 \text{ km s}^{-1}$ . W80 probably assigned this source to the far kinematic distance because of this high-velocity absorption feature. Our H I spectrum for this source shows no 21 cm absorption above  $67 \text{ km s}^{-1}$ . As explained above in § 4.1.3, however, we measure H I absorption up to  $100 \text{ km s}^{-1}$  for another source, G25.397–0.141, which is separated from G25.380–0.181 by only 2'. Because the telescope beamwidth for the D80 survey is also 2', it is likely that the absorption spectrum that they measured toward G25.380–0.181 was substantially contaminated by absorption toward G25.397–0.141. The  $95.7 \text{ km s}^{-1}$  formaldehyde absorption feature that they detected is therefore probably caused by G25.397–0.141 and not by G25.380–0.181, which is the source nearest to the recombination-line emission.

The five remaining discrepancies (G23.437–0.207, G23.691+0.207, G24.469+0.491, G49.370–0.302, and G49.480–0.386) probably arise from our use of different rotation curves. The KDA resolutions in W80 were made using the Schmidt (1965) model of Galactic rotation, whereas we used the C85 rotation curve. We assign G49.370–0.302 to the far kinematic distance and G49.480–0.386 to the tangent-point distance, both with qualities of A, and the other three sources all receive qualities of B. We assign G23.437–0.207 to the near kinematic distance and G23.691+0.207 and G24.469+0.491 to the far kinematic distance. W80, on the other hand, assigns G49.480–0.386 to the far kinematic distance and the other four sources to the tangent-point distance. All five of these H II region complexes have recombination-line velocities within  $10 \text{ km s}^{-1}$  of the tangent-point velocities indicated by the C85 rotation curve, and so they are all near the tangent-point distance. The Schmidt (1965) model predicts a different set of tangent-point velocities, and this is likely to be the reason for the discrepancies. In any case, for none of these five sources is our distance determination more than 1.6 kpc different from that of W80 (after his distances have been scaled so that  $R_0 = 8.5 \text{ kpc}$ ).

CSS88 estimate distances for 50 H II region complexes in the first Galactic quadrant (see their Table 4). They selected the near or far kinematic distance by calculating the density of molecular gas at both locations. In order to do this, they had to first resolve the KDA for the gas itself. They assumed that the latitude profile of the molecular emission at a given longitude and velocity could be modeled by two superposed Gaussian distributions: a narrow component from the gas at the far kinematic distance and a broad component from the gas at the near kinematic distance. The H II region complexes were assigned to the distance that corresponded to a higher molecular gas density. We detect eight of the H II region complexes in their list.

Our near-far determinations agree with those of CSS88 for only one of the sources common to both studies. For the remaining seven sources, our methods yield different results. One of these discrepancies, G28.652+0.027, is probably due to a difference between the criteria used to select tangent-point sources. We assigned this source to the far kinematic distance with a quality of B, and CSS88 assigned it to the tangent-point distance. The recombination-line velocity for this source is only a few  $\text{km s}^{-1}$  below the tangent-point velocity for this line of sight, and our distance determinations actually differ by only 600 pc.

For the six discrepancies that remain (G19.610–0.235, G23.437–0.207, G23.955+0.150, G26.544+0.413, G34.255+0.145, and G43.186–0.526), either we assign the source to the near kinematic distance and CSS88 assign it to the far kinematic distance, or vice versa. We assign a quality of A to all but one of these distance determinations, that of G23.437–0.207.

Because of the small overlap ( $\sim 15\%$ ) between our survey sample and that of CSS88, we cannot be certain whether these six discrepancies characterize a general disparity between the two methods of resolving the KDA. The 75% disagreement rate for sources common to both surveys does suggest, however, that the CSS88 KDA resolutions may be unreliable.

#### 4.3. Correlation with Molecular Gas

Star formation occurs predominately within molecular clouds. Because H II regions are produced by short-lived, early-type stars, there should be a correlation between concentrations of molecular gas and H II regions.

In order to search for such a correlation, we superposed the 49 H II region complexes for which we determined kinematic distances on a kinematically derived profile of the face-on Galactic distribution of molecular hydrogen density (as traced by  $^{12}\text{CO}$  emission) made by CSS88. This is shown in Figure 8. The error bars in position have been calculated as described above in § 3.3.

There are two versions of the C85 rotation curve, one valid for  $R_0 = 8.5$  kpc,  $V_0 = 220$   $\text{km s}^{-1}$ , and another valid for  $R_0 = 10$  kpc,  $V_0 = 250$   $\text{km s}^{-1}$ . We determined kinematic distances using the former version, but the density profile was created using the latter, and in Figure 8, it has been rescaled so that  $R_0 = 8.5$  kpc. The two C85 rotation curves, however, are not scaled versions of one another, and it is not strictly correct to compare this rescaled density profile with the H II region positions from Figure 6. We therefore recalculated the kinematic distances for the 49 H II region complexes using the  $R_0 = 10$  kpc,  $V_0 = 250$   $\text{km s}^{-1}$  version of the C85 rotation curve and then rescaled them so that  $R_0 = 8.5$  kpc. These rescaled distances are typically less than 1% different from the distances in Table 1. In Figure 8, we plot the face-on positions of H II regions derived from these rescaled distances.

A striking correlation is evident between the distribution of H II regions and the main ridges of  $\text{H}_2$  density. The molecular ring is particularly well defined by an arc of 25 H II regions at a Galactocentric radius of 5 kpc. The Sagittarius spiral arm (CSS88) is clearly outlined by an arc of 22 sources at a Galactic radius of roughly 6 kpc, and there is a distinct gap between this feature and the ring. The two sources near a radius of 8 kpc lie on the Perseus spiral arm (CSS88). The spatial correlation between large-scale molecular gas den-

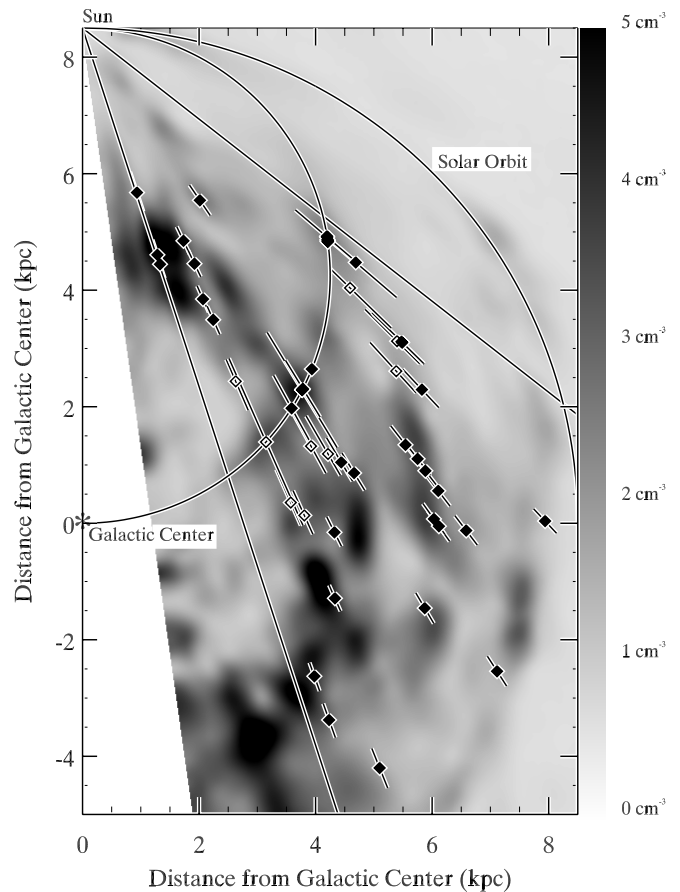


FIG. 8.—Positions of the 49 H II region complexes for which we resolved the KDA, superposed on a gray-scale representation of a kinematically derived molecular hydrogen density profile adapted from CSS88. The original profile has been rescaled so that  $R_0 = 8.5$  kpc, and the gray-scale bar at the right displays the density-color transfer function. Sources with quality A kinematic distance determinations are marked with filled squares, and those with quality B kinematic distance determinations are marked with open squares. The two main arcs of H II region complexes coincide with large-scale features in the density model.

sity peaks and concentrations of bright H II region complexes supports the idea that spiral arms are sites of current star formation.

It is important to emphasize, however, that the distances to these 49 sources were derived from the same Galactic rotation model that was used to determine the molecular hydrogen density distribution. In this light, the excellent face-on correlation can be interpreted more purely as a correlation in  $(l, v)$ -space combined with a successful resolution of the KDA.

#### 4.4. Near-Far Asymmetry

In our sample of 51 H II region complexes, there are  $\sim 3$  times more sources at the far kinematic distance than at the near kinematic distance. This asymmetry could be caused by several effects: geometrical dilution, Malmquist bias, and nonuniform source distribution.

Geometrical dilution is of primary importance. In the inner Galaxy, the area of the disk on the near side of the locus of tangent points is one-third the area on the far side. Therefore, if the sources are distributed uniformly, we expect to find roughly a 3 : 1 ratio between the number of

far and near sources. In addition, because our observations were limited to Galactic latitudes between  $-0^{\circ}5$  and  $+0^{\circ}5$ , we should expect an even larger asymmetry. If the H II region complexes are distributed uniformly in the disk with a Gaussian vertical distribution and a scale height of 50 pc, then our latitude range samples less than 1 scale height for distances closer than 5.7 kpc. The tangent point for our longitude range is, on average, 7.4 kpc away, significantly more distant than the point beyond which we sample a full scale height of the disk. Therefore, our latitude limits cause us to miss significantly more near sources than far sources. Including the effects of both our longitude and latitude ranges, we estimate a total geometrical asymmetry of 3.8 : 1.

Because our source sample is flux-limited, it is subject to Malmquist bias. We could be biased to the detection of intrinsically bright sources, which are rare and typically very distant. The magnitude of such an effect depends on the detailed shape of the radio luminosity function for H II region complexes.

Finally, the asymmetry could partly reflect a genuinely nonuniform distribution of sources. Specifically, there may be an overabundance of H II region complexes at the far kinematic distance in the longitude range of our survey.

The observed asymmetry between H II region complexes at the near and far kinematic distances is easily accounted for by geometrical effects alone. We therefore conclude that the survey geometry is primarily responsible for the observed asymmetry. Both Malmquist bias and a genuine far-side overabundance may exist at a low level, but these effects are probably outweighed by the dominant impact of geometrical asymmetry.

## 5. SUMMARY

We resolved the kinematic distance ambiguity (KDA) toward 49 bright, compact radio H II region complexes in

the first Galactic quadrant by evaluating the maximum velocity of 21 cm H I absorption. With the KDA removed, we were then able to derive kinematic distances to these 49 H II region complexes using their published radio recombination-line velocities.

Most of our KDA resolutions are in agreement with previous determinations. In 22 cases, however, our resolution of the KDA is different from that of previous studies. Where there is disagreement, we believe that our determinations are more reliable. This statement is based on three important factors that affect the quality of our KDA resolutions: the ubiquity of H I clouds, the high spatial resolution of our data, and the ability of the VLA to resolve out large-scale H I emission.

We found  $\sim 3$  times as many sources at the far side of the locus of tangent points as at the near side. This asymmetry can be explained by the geometrical effects of the location of the tangent-point locus and the limited latitude range sampled.

The kinematic distances we determined were used to produce a face-on map of H II region complexes in the first Galactic quadrant. Most of the 49 H II region complexes are concentrated in two main rings with a distinct gap between them. The distribution strongly suggests spiral structure, and the two rings of H II region complexes roughly match the positions of spiral arms proposed by Vallée (2002). Furthermore, the spatial distribution of H II region complexes is strongly correlated with a kinematically derived profile of the density of molecular gas determined from  $^{12}\text{CO}$  emission. The 5 kpc molecular ring and the Sagittarius spiral arm are very distinct, and a few H II region complexes lie along the Perseus arm.

This work was supported in part by NSF grants AST 98-00334 and AST 00-98562. The FCRAO is supported by NSF grants AST 97-25951 and AST 01-00793.

## REFERENCES

- Bania, T. M., & Lockman, F. J. 1984, *ApJS*, 54, 513  
 Blitz, L., Fich, M., & Stark, A. A. 1980, in *IAU Symp. 87, Interstellar Molecules*, ed. B. H. Andrew (Dordrecht: Reidel), 213  
 Brand, J., & Blitz, L. 1993, *A&A*, 275, 67  
 Broadbent, A., Haslam, C. G. T., & Osborne, J. L. 1989, *MNRAS*, 237, 381  
 Clemens, D. P. 1985, *ApJ*, 295, 422 (C85)  
 Clemens, D. P., Sanders, D. B., & Scoville, N. Z. 1988, *ApJ*, 327, 139 (CSS88)  
 Condon, J. J., Cotton, W. D., Greisen, E. W., Yin, Q. F., Perley, R. A., Taylor, G. B., & Broderick, J. J. 1998, *AJ*, 115, 1693  
 Dickey, J. M., & Lockman, F. J. 1990, *ARA&A*, 28, 215  
 Downes, D., Wilson, T. L., Bieging, J., & Wink, J. 1980, *A&AS*, 40, 379 (D80)  
 Kolpak, M. A., Jackson, J. M., Bania, T. M., & Dickey, J. M. 2002, *ApJ*, 578, 868  
 Kuchar, T. A., & Bania, T. M. 1994, *ApJ*, 436, 117 (KB94)  
 Kulkarni, S. R., & Heiles, C. 1987, in *Interstellar Processes*, ed. D. J. Hollenbach & H. A. Thronson, Jr. (Dordrecht: Reidel), 87  
 Liszt, H. S., & Burton, W. B. 1983, in *Kinematics, Dynamics, and Structure of the Milky Way*, ed. W. L. H. Shuter (Dordrecht: Reidel), 135  
 Lockman, F. J. 1989, *ApJS*, 71, 469 (L89)  
 McGlynn, T., Scollick, K., & White, N. 1996, in *IAU Symp. 179, New Horizons from Multiwavelength Sky Surveys*, ed. B. J. McLean et al. (Dordrecht: Kluwer), 465  
 Olling, R. P., & Merrifield, M. R. 1998, *MNRAS*, 297, 943 (OM98)  
 Payne, H. E., Salpeter, E. E., & Terzian, Y. 1983, *ApJ*, 272, 540  
 Perryman, M. A. C., et al. 1995, *A&A*, 304, 69  
 Sault, R. J., Teuben, P. J., & Wright, M. C. H. 1995, in *ASP Conf. Ser. 77, Astronomical Data Analysis Software and Systems IV*, ed. R. Shaw, H. E. Payne, & J. J. E. Hayes (San Francisco: ASP), 433  
 Schmidt, M. 1965, in *Galactic Structure*, ed. A. Blaauw & M. Schmidt (Chicago: Univ. Chicago Press), 513  
 Simon, R., Jackson, J. M., Clemens, D. P., Bania, T. M., & Heyer, M. H. 2001, *ApJ*, 551, 747  
 Steer, D., Dewdney, P., & Ito, M. 1984, *A&A*, 137, 159  
 Vallée, J. 2002, *ApJ*, 566, 261  
 Wilson, T. L. 1972, *A&A*, 19, 354  
 ———. 1980, in *Radio Recombination Lines*, ed. P. A. Shaver (Dordrecht: Reidel), 205 (W80)  
 Wood, D. O. S., & Churchwell, E. 1989, *ApJS*, 69, 831 (WC89)